Phys. Status Solidi A **211,** No. 3, 531–535 (2014) / **DOI** 10.1002/pssa.201330362

physica status solidi a
www.pss-a.com
applications and materials science

Advanced Materials Physics

Origin of broad luminescence from site-controlled InGaN nanodots fabricated by selective-area epitaxy

L. K. Lee[1], L. K. Aagesen[2], K. Thornton[2], and P.-C. Ku[*,1]

[1] Department of Electrical Engineering and Computer Science, University of Michigan, 1301 Beal Ave., Ann Arbor, MI 48109, USA
[2] Department of Materials Science and Engineering, University of Michigan, 2300 Hayward St., Ann Arbor, MI 48109, USA

Received 15 October 2013, revised 4 December 2013, accepted 9 December 2013
Published online 6 February 2014

Keywords gallium nitride, morphology, phase-field model, selective area epitaxy

[*] Corresponding author: e-mail peicheng@umich.edu, Phone: +1 (734) 764 7134, Fax +1 (734) 763 9324

We investigated the origin of broad luminescence observed from an array of site-controlled InGaN nanodots grown by selective area epitaxy (SAE). Epitaxially grown site-controlled nanodots with lateral dimensions <50 nm and an array density of 10^{10} cm^{-2} have been studied. During the nanoscale SAE, incorporation of adatoms from the SiO_2 mask has greater relative importance, resulting in a non-uniform growth profile. This non-uniform growth profile leads to significant broadening of the InGaN nano-heterostructure luminescence. Later in the SAE process, an orientation-dependent growth rate coalesces various crystal planes and transforms these nanostructures into a more uniform array.

1 Introduction III-nitride nanostructures possess unique properties, such as a wide tuning range for the emission wavelength [1, 2] large exciton binding energy (≥26 meV in bulk) [3, 4], and robust spin coherence [5], making them particularly attractive for applications in nanophotonics [6, 7], spintronics [5, 8], and quantum information processing [7, 9]. In many of these applications, it is critical to be able to control the dimension and location of the nanostructures. For example, exciton–cavity coupling requires the precise placement of a single quantum dot heterostructure at the anti-node of an optical cavity [10]. To date, most of the III-nitride nanostructures have been fabricated by the self-assembled Stranski–Krastanow (SK) growth [11], which does not enforce control over the structures' position or dimension, demotivating their practical use on the device level. In recent years, selective area epitaxy (SAE) using metal-organic chemical vapor deposition (MOCVD) has been proven to be feasible for the fabrication of a variety of site-controlled III-nitride nanostructures, such as nanowires [12] and nanodots [2, 13–18]. During SAE, the morphology of the three-dimensional epistructure grown within the mask opening evolves according to the growth dynamics [12, 19], source supply mechanisms [20, 21], and growth rate anisotropy [22, 23]. Because optical properties of III-nitride heterostructures strongly depend on the anisotropic piezoelectric fields [2, 19, 24–27], it is important to understand and control the morphology of each epitaxial layer in SAE. In this paper, we study the growth profile evolution of a high-density site-controlled III-nitride nanodot array with sub-50 nm diameters, both theoretically and experimentally.

2 Experimental

2.1 Nanostructure growth Figure 1 shows site- and dimension-controlled InGaN nanodots fabricated by two different methods, one by SAE and the other by top–down etching of an InGaN single quantum well (SQW) into nanopillars. The sample preparation for the SAE-grown structures is as follows. First, a 1.5-μm thick GaN template was epitaxially grown on a c-plane sapphire substrate at 1050 °C with a 25 nm low-temperature nucleation layer. A 40 nm thick SiO_2 layer was then *ex situ* deposited by plasma-enhanced chemical vapor deposition. The SiO_2 layer was patterned into an array of nanoscale holes with diameters of 25 nm for the subsequent SAE using electron-beam lithography (Raith 150 with PMMA resist) and reactive ion etching (Oxford Instruments PlasmaTherm 790).

The spacing between two adjacent nanoholes was fixed at 100 nm, giving an array density of 10^{10} cm^{-2}. After the removal of the PMMA resist by acetone and oxygen plasma

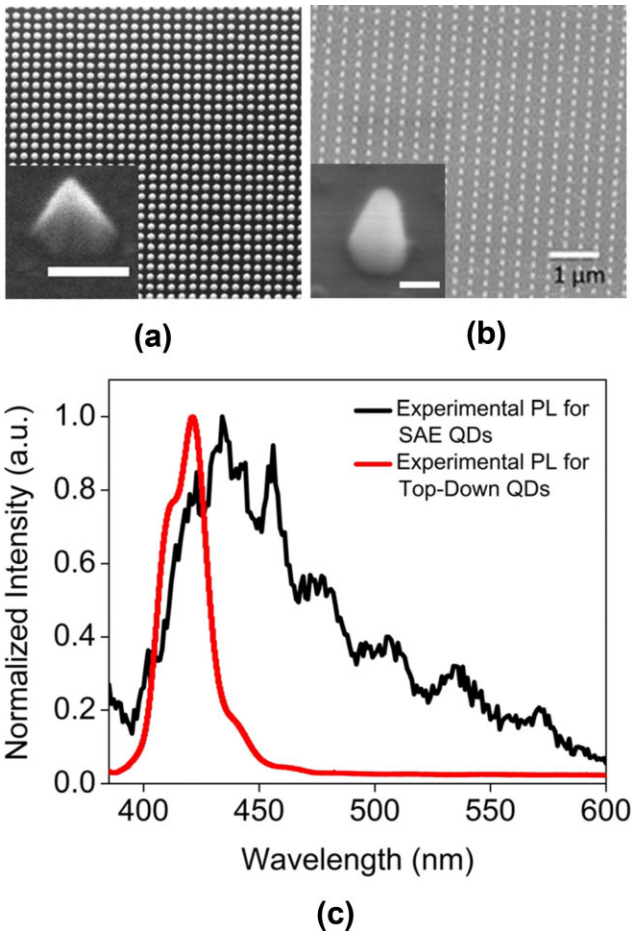

Figure 1 SEM images of the InGaN quantum dot arrays fabricated by (a) nanoscale SAE and by (b) top–down etching. Insets are the zoomed-in SEM view of individual nanostructures in the arrays; both scale bars in the insets represent 50 nm. (c) Room-temperature PL spectra of the InGaN quantum dot arrays fabricated by the two approaches.

ashing, the sample was transferred to a Thomas-Swan closed-coupled showerhead MOCVD system for SAE. The InGaN nanodots were deposited within the 25-nm-diameter aperture. The deposition rate of GaN/InGaN was adjusted according to the pattern's fill-factor [20, 21, 28] to aim for 20 nm nominal GaN thickness, followed by 3-nm nominal InGaN thickness at nominal indium composition of 15%, followed by GaN capping. Once the cap GaN layer grew beyond the aperture, the morphology became dominated by different growth rates along different crystallographic orientations. As a result, the slowest-growing plane emerged at the end. As for the top-down etched sample, an InGaN SQW with 3-nm well width was patterned with 25-nm-diameter Cr nanodots as etch masks, whose lateral dimension passed down to the nanopillars after RIE, and hence the 25-nm-diameter InGaN quantum disks were embedded in the nanopillars.

2.2 Nanostructure morphology and optical characterization Both samples were imaged by scanning electron microscopy and displayed a uniform array as shown in Fig. 1a and b for the SAE and top–down etched samples, respectively. The variation of the dot's lateral dimension in both samples was less than 5 nm. To measure the optical properties of these two samples, a total of 10^4 nanodots were excited at room temperature using a 390-nm wavelength pulsed laser (130 fs). The beam spot was intentionally controlled at 30 μm diameter on the sample surface in order to cover the entire 10 μm × 10 μm nanodot array. The optical intensity was estimated to be 5 kW cm^{-2}. The photoluminescence (PL) spectra of these two samples are plotted in Fig. 1c. Despite the seemingly identical and uniform InGaN nanodot dimensions in these two samples by design, the FWHM linewidth of the etched array is less than half of that of the SAE array (350 meV). We attributed the large linewidth difference to the difference in nanodot shapes. For the etched sample, the uniform 3-nm quantum well width does not leave much room for variation, while in SAE, because of the evolving growth profile, the morphology of the InGaN layer can significantly alter the output optical properties. To verify this assertion, we have developed a phase-field model to describe the growth morphology evolution during SAE.

3 Phase-field model We simulated the growth evolution during nanoscale SAE by the phase-field method, where the value of an order parameter φ differentiates between the film and vapor phases. The order parameter evolves via the Cahn–Hilliard equation, modified to enforce a fixed contact angle boundary condition at the vapor–solid–SiO_2 three-phase boundary using the smoothed boundary method (SBM) [29, 30]. The position of the SiO_2 mask is represented by a domain parameter, ψ, which varies smoothly between 0 and 1. The three phases of the system are represented by: $\psi = 0$, $\varphi = 0$, mask; $\psi = 1$, $\varphi = 0$, vapor; $\psi = 1$, $\varphi = 1$, GaN (or InGaN, which is assumed to have identical material properties for the purpose of phase-field modeling). Deposition from the vapor and from surface diffusion of adatoms from the mask are modeled using source terms, and the concentration of precursor gases in the vapor phase is assumed constant over the surface of the growing nanostructure. The SBM-modified Cahn–Hilliard equation [31] with the addition of source terms for deposition [32] is

$$\frac{\partial \varphi}{\partial t} = \frac{1}{\psi}\nabla \cdot [\psi M(\varphi)\nabla \mu] + d_{\mathrm{v}} v(\alpha)\varphi^2(1-\varphi)^2 + d_{\mathrm{TPB}}\varphi^2(1-\varphi)^2\psi^2(1-\psi)^2, \quad (1)$$

$$\mu = \frac{\partial f}{\partial \varphi} - \frac{\varepsilon^2}{\psi}\left(\nabla \cdot (\psi \nabla \varphi)\frac{|\nabla \psi|\sqrt{2f}}{\varepsilon}\cos\theta\right), \quad (2)$$

where $M(\varphi) = \varphi^2(1-\varphi)^2$ localizes diffusion to the surface, $f = W_{\mathrm{f}}\varphi^2(1-\varphi)^2$ is of a double-well form with the barrier height controlled by W_{f}, ε^2 is the gradient energy coefficient, θ is the contact angle at the vapor–solid–SiO_2 triple point (set

at 135°, which was experimentally measured), d_v is the rate of deposition from the vapor directly to the nanodot surface, $v(\alpha)$ accounts for the anisotropy of deposition rate as a function of the angle α between the interface and the [0001] direction in the $(11\bar{2}0)$ plane (taken from [33]), and d_{TPB} is the deposition rate of adatoms that diffuse from the mask surface to the nanodot. A two-dimensional cross-section is simulated in the $(11\bar{2}0)$ plane because it contains slow-growing $<1\bar{1}01>$ directions, which are normal to the $\{1\bar{1}01\}$ planes that bound the hexagonal pyramidal shape at the completion of growth [33]. We model the deposition due to adatoms from the mask as localized to the vapor–solid–SiO_2 three-phase boundary as in [34] using the terms $\varphi^2(1-\varphi)^2\psi^2(1-\psi)^2$ and assume that d_{TPB} is constant throughout the deposition process because the distance between nanodot edges changes very little during these early stages of deposition (we ignore the transient during the very early phase).

4 Comparison of simulations and experimental results

4.1 Nanostructure morphology To validate the above model, we grew GaN nanodots again at 760 °C using SAE with the same pattern geometry, but interrupted the growth at different times. The as-grown samples were imaged as shown in Fig. 2, with growth interrupted at 1, 2, and 3 min. As a comparison, we simulated growth using the phase-field model with the following parameters: $\varepsilon = 1$, $W_f = 1$, a grid size of 300×300, grid spacing $\Delta x = 1$, and time step $\Delta t = 2.0$, and varied d_v and d_{TPB}. The results exhibit a good agreement with the experimental observations as shown in Fig. 2 using $d_v = 0.00093$ and $d_{TPB} = 0.33$, reproducing the volcano-like shape in the early stage and predicting an emergence of the facets with slow growth at the later stage of the deposition process. Such transitions were not observed unless the deposition onto the mask was accounted for, and were only reproducible within a small range of the parameter sets. In particular, we found that the dewetting contact angle and the specific values of d_v and d_{TPB} were critical in obtaining a morphology consistent with experimental observations.

We interpreted the results shown in Fig. 2 as follows. During SAE, the primary supply of growth species to nanodots occurs through vapor-phase diffusion. In addition to direct deposition from the vapor phase, deposition occurs onto the mask, resulting in adatoms that can be incorporated through surface diffusion or vapor-phase diffusion (after re-evaporation), which can enhance deposition at the edge of the nanodot [21]. This additional flux results in a localized growth rate enhancement (Stage I, Fig. 2). Nanoring structures are observed in this stage [16–18]. As growth proceeded, the effect of growth rate anisotropy started to coalesce different crystal planes around the edge toward the center of the nanoring (Stage II, Fig. 2). Eventually, the slowest growing $\{1\bar{1}01\}$ planes dominated the growth profile, resulting in a hexagonal pyramidal shape (Stage III, Fig. 2).

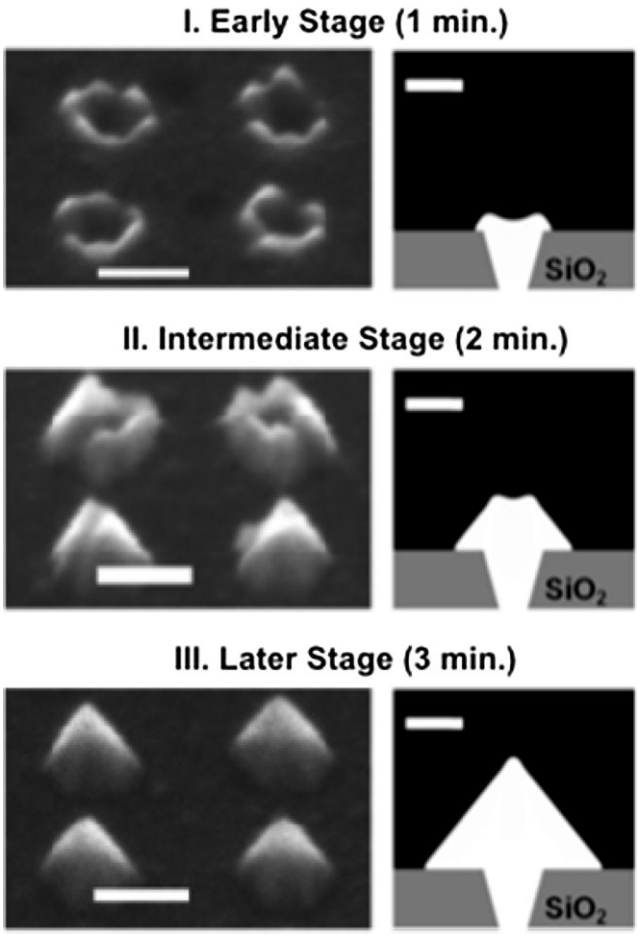

Figure 2 The left shows the SEM images taken at the different stages of the nanoscale SAE and the right shows the calculated morphology. The scale bars on the left and on the right are 50 and 40 nm, respectively.

4.2 Optical performance The results on growth morphology evolution were also used to explain the broad PL linewidth as shown in Fig. 1c. First, we simulated the growth of the InGaN layer using the phase-field model, and from simulation, we calculated the InGaN layer profile as shown by the thick line in the inset of Fig. 3. The thickness of the InGaN layer varied considerably (from about 2 to 6 nm) along the lateral dimension of the nanodot, as a result of the growth rate enhancement at the edge of the nanohole during the early stage of SAE. Using this InGaN layer thickness profile, we calculated the PL spectrum by assuming that the InGaN layer is a quantum well of varying well thickness. We simplified the calculation by assuming the main PL broadening mechanism came from the varying thickness. This was justified by noting that the quantum confinement in the transverse direction is much stronger than that in the lateral direction, which is around 25 nm. We applied the propagation-matrix approach and the spontaneous emission model to calculate the emission spectrum of an SQW with a particular well thickness, as described in Ref. [35]. Material

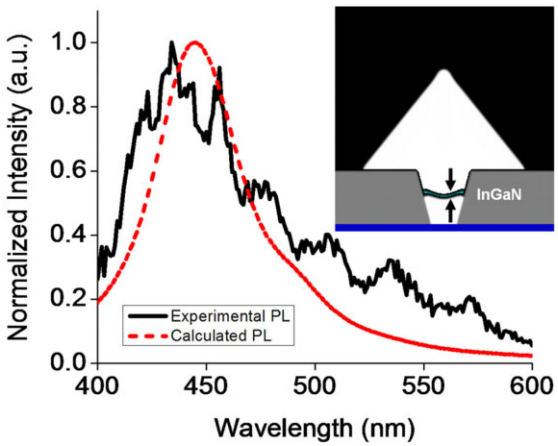

Figure 3 Room-temperature photoluminescence spectrum and the calculated photoluminescence spectrum of the InGaN nanodot array. The calculated PL spectrum is based on the calculated InGaN layer thickness profile shown in the inset. The two lines in the inset represent the InGaN/GaN boundaries.

parameters used in calculation were based on Ref. [36]. The overall calculated PL spectrum is the summation of all the individual SQW emission with a range of well thicknesses (2–6 nm). The quantum-confined Stark effect (QCSE) due to piezoelectric field is modeled by using a tilted quantum well energy profile (potential gradient caused by the electric field) in the SQW calculation. We assumed the internal electric field caused by the piezoelectric polarizations to be 2 MV cm^{-1} along the growth direction, i.e., the *c*-axis. We also adjusted the piezoelectric field based on the direction of narrowest transverse confinement across the quantum well region. The calculated PL is shown in Fig. 3, and it agreed with the measured PL spectrum, except for the "peaks" caused by Fabry–Perot interference originating from the GaN template material in the unpatterned region surrounding the nanodot array. Since the excitation beam spot (30 μm diameter) is larger than the nanodot array (10 μm × 10 μm), Fabry–Perot interference occurs in the GaN template material outside the nanodot array, bounded by the unpatterned SiO_2 on top and the sapphire substrate below.

5 Conclusions In summary, motivated by the broad luminescence from an apparently uniform InGaN nanodot array, we studied the growth profile evolution of a high-density site-controlled III-nitride nanodot array with sub-50 nm diameters. Using the phase-field model, we were able to simulate the growth profile evolution, which agreed with the experimental results. We found that in the initial stage of the nanoscale SAE when the deposition of adatoms from the mask surface locally dominated the direct deposition onto the dot, the growth rate was locally enhanced near the dot edge. This led to non-uniform heterostructure thickness. As a result, the PL of an array of InGaN nanodots exhibited a broad linewidth, in contrast to the apparently uniform dot size. We also asserted that the further reduction of the PL linewidth is possible by controlling the InGaN layer profile based on phase-field simulation.

Acknowledgements The work involving MOCVD growth, the phase-field model, and photoluminescence calculation were supported by the Center for Solar and Thermal Energy Conversion (CSTEC), an Energy Frontier Research Center funded by the U.S. Department of Energy (DOE), Office of Science, Basic Energy Sciences (BES) under Award Number DE-SC0000957. The work involving lithography, SAE mask, and optical measurements were supported by National Science Foundation under Award ECCS 0901477. Part of this work was performed in Lurie Nanofabrication Facility, which is part of the NSF NNIN network.

References

[1] Y. Arakawa and S. Kako, Phys. Status Solidi A **203**, 3512 (2006).
[2] V. Pérez-Solórzano, A. Gröning, M. Jetter, T. Riemann, and J. Christen, Appl. Phys. Lett. **87**, 163121 (2005).
[3] Y. Narukawa, Y. Kawakami, S. Fujita, S. Fujita, and S. Nakamura, Phys. Rev. B **55**, R1938 (1997).
[4] W. Huang and F. Jain, J. Appl. Phys. **87**, 7354 (2000).
[5] B. Beschoten, E. Johnston-Halperin, D. K. Young, M. Poggio, J. E. Grimaldi, S. Keller, S. P. DenBaars, U. K. Mishra, E. L. Hu, and D. D. Awschalom, Phys. Rev. B **63**, 121202(R) (2001).
[6] F. Qian, Y. Li, S. Gradečak, D. Wang, C. J. Barrelet, and C. M. Lieber, Nano Lett. **4**, 1975 (2004).
[7] S. Kako, C. Santori, K. Hoshino, S. Götzinger, Y. Yamamoto, and Y. Arakawa, Nature Mater. **5**, 887 (2006).
[8] S. J. Pearton, Y. D. Park, C. R. Abernathy, M. E. Overberg, G. T. Thaler, J. Kim, and F. Ren, J. Electron. Mater. **32**, 288 (2003).
[9] S. De Rinaldis, I. D'Amico, E. Biolatti, R. Rinaldi, R. Cingolani, and F. Rossi, Phys. Rev. B **65**, 081309 (2002).
[10] G. Khitrova, H. M. Gibbs, M. Kira, S. W. Koch, and A. Scherer, Nature Phys. **2**, 81 (2006).
[11] D. Bimberg, M. Grundmann, and N. N. Ledentsov, Quantum Dot Heterostructures (John Wiley and Sons, West Sussex, 1999), chap. 4.
[12] S. D. Hersee, X. Sun, and X. Wang, Nano Lett. **6**, 1808 (2006).
[13] M. Lachab, M. Nozaki, J. Wang, Y. Ishikawa, Q. Fareed, T. Wang, T. Nishikawa, K. Nishino, and S. Sakai, J. Appl. Phys. **87**, 1374 (2000).
[14] K. Tachibana, T. Someya, S. Ishida, and Y. Arakawa, J. Cryst. Growth **221**, 576 (2000).
[15] P. R. Edwards, R. W. Martin, I. M. Watson, C. Liu, R. A. Taylor, J. H. Rice, J. H. Na, J. W. Robinson, and J. D. Smith, Appl. Phys. Lett. **85**, 4281 (2004).
[16] P. Chen, S. J. Chua, Y. D. Wang, M. D. Sander, and C. G. Fonstad, Appl. Phys. Lett. **87**, 143111 (2005).
[17] Y. Wang, K. Zang, S. Chua, M. S. Sander, S. Tripathy, and C. G. Fonstad, J. Phys. Chem. B **110**, 11081 (2006).
[18] P. Chen, A. Chen, S. J. Chua, and J. N. Tan, Adv. Mater. **19**, 1707 (2007).
[19] S. Srinivasan, M. Stevens, F. A. Ponce, and T. Mukai, Appl. Phys. Lett. **87**, 131911 (2005).
[20] J. Yamaguchi, J. Ogasawara, and K. Okamoto, J. Appl. Phys. **72**, 5919 (1992).
[21] J. Yamaguchi and K. Okamoto, Jpn. J. Appl. Phys. **32**, 1523 (1993).

[22] J. Park, P. A. Grudowski, C. J. Eiting, and R. D. Dupuis, Appl. Phys. Lett. **73**, 333 (1998).
[23] D. Kapolnek, S. Keller, R. Vetury, R. D. Underwood, P. Kozodoy, S. P. Den Baars, and U. K. Mishra, Appl. Phys. Lett. **71**, 1204 (1997).
[24] H. Yu, L. K. Lee, T. Jung, and P.-C. Ku, Appl. Phys. Lett. **90**, 141906 (2007).
[25] A. F. Jarjour, R. A. Oliver, A. Tahraoui, M. J. Kappers, R. A. Taylor, and C. J. Humphreys, Superlattices Microstruct. **43**, 431 (2008).
[26] A. F. Jarjour, R. A. Oliver, and R. A. Taylor, Philos. Mag. **87**, 2077 (2007).
[27] V. Pérez-Solórzano, A. Gröning, H. Schweizer, and M. Jetter, Phys. Status Solidi B **242**, R97 (2005).
[28] L. K. Lee, T. Jung, and P.-C. Ku, IEEE CLEO/QELS, CThS2 (San Jose, CA, 2008).
[29] H.-C. Yu, H.-Y. Chen, and K. Thornton, Model. Simul. Mater. Sci. Eng. **20**, 075008 (2012).
[30] S. Aland, J. Lowengrub, and A. Voigt, Comput. Model. Eng. Sci. **57**, 77 (2010).
[31] H.-Y. Chen, H.-C. Yu, and K. Thornton, J. Power Sources **196**, 1333 (2011).
[32] L. K. Aagesen, L. K. Lee, P.-C. Ku, and K. Thornton, J. Cryst. Growth **361**, 57 (2012).
[33] V. Jindal and F. Shahedipour-Sandvik, J. Appl. Phys. **106**, 083115 (2009).
[34] M. Khenner, R. J. Braun, and M. G. Mauk, J. Cryst. Growth **241**, 330 (2002).
[35] S. L. Chuang, Physics of Optoelectronic Devices (Wiley-Interscience, New York, 1995), pp. 157–160, 345–351.
[36] I. Vurgaftman and J. R. Meyer, J. Appl. Phys. **94**, 3675 (2003).